

# A Model of the Subpacket Structure of Rising Tone Chorus Emissions

Miroslav Hanzelka<sup>1</sup>, Ondrej Santolik<sup>1</sup>, Yoshiharu Omura<sup>2</sup>, Ivana Kolmašová<sup>3</sup>, and Craig A Kletzing<sup>4</sup>

<sup>1</sup>Department of Space Physics Institute of Atmospheric Physics Czech. Acad. Sci. Prague Czech Republic

<sup>2</sup>Research Institute for Sustainable Humanosphere Kyoto University Uji Japan

<sup>3</sup>Department of Space Physics Institute of Atmospheric Physics Czech. Acad. Sci. Prague Czech Republic

<sup>4</sup>Department of Physics and Astronomy University of Iowa Iowa City Iowa USA

November 22, 2022

## Abstract

The nonlinear growth theory of chorus emissions is used to develop a simple model of the subpacket formation. The model assumes that the resonant current, which is released from the source to the upstream region, radiates a new whistler mode wave with a slightly increased frequency, which triggers a new subpacket. Saturation of the growth in amplitude is controlled by the optimum amplitude. Numerical solution of advection equations for each subpacket, with the chorus equations acting as the boundary conditions, produces a chorus element with a subpacket structure. This element features an upstream shift of the source region with time and an irregular growth of frequency, showing small decreases between adjacent subpackets. The influence of input parameters on the number of subpackets, the shift of the source, the frequency sweep rate and the maximum amplitude is analyzed. The model well captures basic features of instantaneous frequency measurements provided by the Van Allen Probes spacecraft. The modeled wave field can be used in future particle acceleration studies.

# A model of the subpacket structure of rising tone chorus emissions

Miroslav Hanzelka<sup>1,2</sup>, Ondřej Santolík<sup>1,2</sup>, Yoshiharu Omura<sup>3</sup>, Ivana Kolmašová<sup>1,2</sup>, Craig A. Kletzing<sup>4</sup>

<sup>1</sup>Department of Space Physics, Institute of Atmospheric Physics, Czech. Acad. Sci., Prague, Czech Republic

<sup>2</sup>Faculty of Mathematics and Physics, Charles University, Prague, Czech Republic

<sup>3</sup>Research Institute for Sustainable Humanosphere, Kyoto University, Uji, Japan

<sup>4</sup>Department of Physics and Astronomy, University of Iowa, Iowa City, Iowa, USA

## Key Points:

- A simple model of subpacket formation in rising tone chorus emissions is presented.
- The model features drops in frequency between subpackets and upstream shift of the source.
- The model compares well with observations made by Van Allen Probes spacecraft in the outer radiation belt.

---

Corresponding author: M. Hanzelka, [mha@ufa.cas.cz](mailto:mha@ufa.cas.cz)

**Abstract**

The nonlinear growth theory of chorus emissions is used to develop a simple model of the subpacket formation. The model assumes that the resonant current, which is released from the source to the upstream region, radiates a new whistler mode wave with a slightly increased frequency, which triggers a new subpacket. Saturation of the growth in amplitude is controlled by the optimum amplitude. Numerical solution of advection equations for each subpacket, with the chorus equations acting as the boundary conditions, produces a chorus element with a subpacket structure. This element features an upstream shift of the source region with time and an irregular growth of frequency, showing small decreases between adjacent subpackets. The influence of input parameters on the number of subpackets, the shift of the source, the frequency sweep rate and the maximum amplitude is analyzed. The model well captures basic features of instantaneous frequency measurements provided by the Van Allen Probes spacecraft. The modeled wave field can be used in future particle acceleration studies.

**1 Introduction**

Chorus emissions are coherent electromagnetic waves propagating in the whistler mode which are frequently observed in the inner magnetosphere, typically in the range of L-shells from 4 to 8 (Tsurutani & Smith, 1974; Santolík, Gurnett, et al., 2003; Kasahara et al., 2009). They can induce both acceleration and losses of energetic electrons in the radiation belts (Tsurutani et al., 2009; Turner et al., 2013) through nonlinear interactions (Summers et al., 2013). These processes are sensitive to the frequency-time structure of the chorus wave packets (Tao et al., 2013), which therefore needs to be well understood in order to fully comprehend the dynamics of the radiation belts. The fine structure of chorus elements which rise in frequency has been discovered from high resolution measurements of the Cluster spacecraft (Santolík, Gurnett, et al., 2003; Santolík et al., 2004) which show that each element of the discrete emission consists of several subpackets with growing wave frequencies. The subpacket structure of chorus has been confirmed by recent analyses of multi-component measurements of chorus by Van Allen Probes (Santolík, Kletzing, et al., 2014; Foster et al., 2017; Omura et al., 2019). This fine structure has also been observed in full particle simulations (Hikishima et al., 2009, 2010) and hybrid simulations (Katoh & Omura, 2016). A feature unique to the simulations, not

47 yet observed by any spacecraft missions, is the movement of the source to the region up-  
 48 stream of the wave, which happens along the frequency growth.

49 To explain the features of chorus emissions discovered in numerical simulations and  
 50 spacecraft measurements, the nonlinear growth theory has been developed (Omura et  
 51 al., 2008, 2009). This theory recognizes the inhomogeneity of magnetic field along a field  
 52 line as the main controlling factor for the formation of an electromagnetic electron hole  
 53 in the velocity phase space. Phase-bunched resonant electrons traveling around the hole  
 54 produce a resonant current which causes the amplitude and frequency growth of the whistler  
 55 mode wave. The nonlinear growth theory gives values of frequency sweep rates and am-  
 56 plitudes of chorus elements which are in good agreement with in situ observations (Kurita  
 57 et al., 2012; Yagitani et al., 2014; Foster et al., 2017). It has also been applied to explain  
 58 the fine structure of electromagnetic ion cyclotron (EMIC) emissions, which, similarly  
 59 to chorus, consist of several subpackets (Omura et al., 2010; Nakamura et al., 2015). The  
 60 subpacket structure of EMIC waves was analyzed numerically by Shoji and Omura (2013)  
 61 and they also presented an idea that the subpackets could be produced by a repeated  
 62 triggering process caused by the radiation from phase-organized protons which are con-  
 63 tinuously being released from the interaction region.

64 In the present study we use the nonlinear growth theory to develop a simple model  
 65 of the fine structure of rising tone chorus emission, taking inspiration from the idea of  
 66 subpacket formation in EMIC waves presented by Shoji and Omura (2013). The evolu-  
 67 tion of the wave amplitude and wave frequency inside a single subpacket in the source  
 68 region is described by the so-called chorus equations, derived by Omura et al. (2009).  
 69 Wave propagation and convective growth is modeled with advection equations. The fun-  
 70 damental assumption employed in the present model is that the resonant current, pro-  
 71 duced through wave-particle interaction, carries the information about the wave vector  
 72 and frequency of the emission and can act as a helical antenna and radiate a new coher-  
 73 ent wave during their upstream propagation. Similar idea (i.e., the resonant current act-  
 74 ing as an antenna) already appeared in the seminal paper of Helliwell (1967), but they  
 75 did not connect it with the nonlinear growth theory, which was not yet fully developed  
 76 at that time. Trakhtengerts et al. (2003) analyzed the frequency shift due to this antenna  
 77 effect and estimated the amplitude of the emitted radiation, however, they did not con-  
 78 sider it as a possible cause for the subpacket structure. Here, some further assumptions  
 79 are made to separate the newly radiated wave from the previous subpacket, and the op-

80 timum amplitude derived by Omura and Nunn (2011) is used to introduce saturation  
 81 effects into the model. Chorus elements obtained from the numerical solution show that  
 82 between adjacent subpacket, there are small, local drops in the otherwise growing fre-  
 83 quency, which is a feature that seems to be also indicated by the measurements of the  
 84 Van Allen Probes (Santolík, Kletzing, et al., 2014; Foster et al., 2017). The upstream  
 85 shift of the source region, previously obtained in some full-particle simulations, is also  
 86 present in the model.

87 This new model of the subpacket structure of the chorus emission is introduced in  
 88 Section 2, which is further divided into three subsections that deal with the evolution  
 89 equations for chorus, the resonant current and the proposed sequence of processes that  
 90 occur during the growth of a chorus element. In Section 3 we present the numerical so-  
 91 lution of the differential equations describing the new model, focusing on its unique fea-  
 92 tures, namely the movement of the source region to the upstream and the inversion of  
 93 frequency growth between subpackets. Section 4 is dedicated to the comparison of the  
 94 modeled chorus element with Van Allen Probes observations of rising tone chorus emis-  
 95 sions in the radiation belts. In Section 5 and we further discuss the advantages and short-  
 96 comings of the presented model and conclude our main results.

## 97 2 Model of a chorus element

### 98 2.1 The evolution equations

99 We are studying the evolution of wave frequency  $\omega(h, t)$  and wave amplitude  $B_w(h, t)$   
 100 of a coherent electromagnetic whistler mode wave propagating parallel to a background  
 101 dipole magnetic field through a one-component plasma with a constant number density  
 102 of electrons. Distance  $h$  is measured along a magnetic field line, starting at the equator,  
 103  $t$  is the time. Following Summers et al. (2012), we describe the evolution with two cou-  
 104 pled advection equations

$$105 \frac{\partial \omega}{\partial t} + V_g \frac{\partial \omega}{\partial h} = 0, \quad (1)$$

$$106 \frac{\partial B_w}{\partial t} + V_g \frac{\partial B_w}{\partial h} = -\frac{\mu_0 V_g}{2} J_E, \quad (2)$$

108 where  $V_g$  is the group velocity of a whistler mode wave,  $\mu_0$  is the permeability of vac-  
 109 uum and  $J_E$  is the resonant current density component parallel to the wave electric field.  
 110 The first equation simply states that the frequency is constant in a frame of reference  
 111 moving with the group velocity, which is a consequence of the ray approximation (Lighthill,

112 1965). A detailed derivation of the second equation has been given by, e.g., Nunn (1974)  
 113 or Omura et al. (2008). Following Foster et al. (2017), we use Equations 1 and 2 to de-  
 114 scribe the evolution of a single subpacket, not the whole chorus element, which was done  
 115 in previous studies, e.g. Summers et al. (2012).

116 The time evolution of  $B_w$  and  $\omega$  in the source is given by the chorus equations of  
 117 Omura et al. (2009). To obtain the equation for  $\omega$ , we start from the definition of the  
 118 inhomogeneity ratio

$$119 \quad S = -\frac{1}{s_0\omega\Omega_w} \left( s_1 \frac{\partial\omega}{\partial t} + cs_2 \frac{\partial\Omega_e}{\partial h} \right), \quad (3)$$

120 where  $\Omega_w$  is the normalized wave amplitude defined by  $\Omega_w = eB_w/m_e$ ,  $e$  denotes the  
 121 elementary charge,  $m_e$  denotes the electron rest mass and  $c$  is the speed of light in vac-  
 122 uum. The explicit forms of parameters  $s_0$ ,  $s_1$  and  $s_2$  are given in Omura et al. (2009),  
 123 Eq. 11 – 13. Further we will assume a parabolic approximation of the magnetic field strength  
 124 along field lines, allowing us to define the dependence of electron gyrofrequency on the  
 125 distance along field line as

$$126 \quad \Omega_e = \Omega_{e0} (1 + ah^2), \quad (4)$$

127 where  $\Omega_{e0} = eB_{eq}/m_e$  is the equatorial electron gyrofrequency,  $B_{eq}$  is the magnetic field  
 128 strength at the equator and  $a$  comes from the small-latitude Taylor expansion of the mag-  
 129 netic field and is given by  $a = 4.5/(LR_E)^2$ , with  $R_E$  being the Earth's radius. Conse-  
 130 quently,

$$131 \quad \frac{\partial\Omega_e}{\partial h} = 2ah\Omega_{e0}. \quad (5)$$

132 We will require that  $|J_E|$  is maximized in the source, which is located in the distance  $h_i$ ,  
 133 where  $i$  indexes the subpackets. The maximum of  $|J_E|$  is achieved with (Omura et al.,  
 134 2008)  $S \approx -0.41 \equiv -S_{\max}$ . We can now substitute this value on the left hand side of  
 135 Equation 3 to obtain, using also Equation 5, the first chorus equation

$$136 \quad \left. \frac{\partial\omega}{\partial t} \right|_{h_i} = \frac{S_{\max}s_0\omega}{s_1}\Omega_w - \frac{2ach_i s_2}{s_1}\Omega_{e0}. \quad (6)$$

137 The second term on the right hand side is not present in the derivation of similar equa-  
 138 tion presented in Omura et al. (2009), because in Equation 6 we have allowed the source  
 139 to be located away from the equator.

140 The second chorus equation uses the concept of the threshold amplitude, which re-  
 141 mains unchanged for  $h_i \neq 0$ , so we can write (Omura et al., 2009)

$$142 \quad \left. \frac{\partial\Omega_w}{\partial t} \right|_{h_i} = \Gamma_N\Omega_w - \frac{2acV_g s_2}{S_{\max}s_0} \frac{\Omega_{e0}}{\omega}. \quad (7)$$

143 Here  $\Gamma_N$  represents the growth rate defined by

$$144 \quad \frac{\partial \Omega_w}{\partial t} + V_g \frac{\partial \Omega_w}{\partial h} = \frac{d\Omega_w}{dt} \equiv \Gamma_N \Omega_w. \quad (8)$$

145 As we will show in the next subsection,  $\Gamma_N$  depends on both  $\Omega_w$  and  $\omega$ , which causes a  
146 strongly nonlinear growth.

## 147 2.2 Resonant current

148 The interaction between resonant electrons and whistler mode waves leads to the  
149 depletion of trapped electrons from the phase space, which is often called the electro-  
150 magnetic electron hole (Omura & Summers, 2006). Untrapped particles traveling around  
151 the hole experience phase bunching (Helliwell, 1967; Dysthe, 1971), which manifests through  
152 the appearance of the resonant current density  $J_R$ . It is useful to decompose this cur-  
153 rent density into the components  $J_E$  and  $J_B$  which are parallel to the wave electric and  
154 magnetic fields, respectively. The  $J_E$  component is connected to the growth of wave am-  
155 plitude, as we have seen in Equation 2, and  $J_B$  causes the growth of wave frequency. They  
156 may be expressed as (Omura et al., 2008)

$$157 \quad J_E = -J_0 \int_{\zeta_1}^{\zeta_2} (\cos \zeta_1 - \cos \zeta + S(\zeta - \zeta_1))^{\frac{1}{2}} \sin \zeta \, d\zeta, \quad (9)$$

$$158 \quad J_B = J_0 \int_{\zeta_1}^{\zeta_2} (\cos \zeta_1 - \cos \zeta + S(\zeta - \zeta_1))^{\frac{1}{2}} \cos \zeta \, d\zeta, \quad (10)$$

160 where  $\zeta$  is the gyrophase angle defined with respect to the wave magnetic field, and  $\zeta_1(S)$ ,  
161  $\zeta_2(S)$  set the left and right boundaries of the separatrix in the  $v_{\parallel}(\zeta)$  phase portrait. The  
162 quantity  $J_0$  depends on the distribution of hot electrons trapped by the wave. Here we  
163 follow Summers et al. (2012) and assume a fully adiabatic evolution of a hot electron dis-  
164 tribution, chosen to be bi-Maxwellian in momenta, to define

$$165 \quad J_0 = \frac{(2^3 e^3 V_{\perp 0}^5 B_w)^{\frac{1}{2}}}{(m_e k \gamma_R)^{\frac{1}{2}}} \chi Q G, \quad (11)$$

166 where

$$167 \quad G(h) = \left( \frac{1 + ah^2}{1 + ah^2(1 + A_{\text{eq}})} \right)^{\frac{1}{2}} \frac{N_{\text{he}}}{2\pi^2 U_{\text{th},\perp\text{eq}} U_{\text{th},\parallel\text{eq}}} \exp \left( -\frac{\gamma_R^2 V_R^2}{2U_{\text{th},\parallel\text{eq}}^2} \right) \quad (12)$$

168 carries information about the distribution function and

$$169 \quad A_{\text{eq}} = \frac{U_{\text{th},\perp\text{eq}}^2}{U_{\text{th},\parallel\text{eq}}^2} - 1 \quad (13)$$

170 is the equatorial anisotropy of the hot electron distribution. The other quantities we in-  
171 troduced in Equations 11 and 12 are as follows: average perpendicular electron veloc-

172 ity  $V_{\perp 0}$ , wave number  $k$ , resonance velocity  $V_R$ , Lorentz factor  $\gamma_R$  of an electron prop-  
 173 agating with the resonance velocity, dimensionless parameter  $\chi^2 = 1 - \omega^2/c^2k^2 = 1 - 1/n^2$   
 174 (where  $n$  is the refractive index of a whistler mode wave), number density  $N_{\text{he}}$  of the hot  
 175 electron population, depth of the electron hole  $Q$ , equatorial perpendicular thermal ve-  
 176 locity  $U_{\text{th},\perp\text{eq}}$  and equatorial parallel thermal velocity  $U_{\text{th},\parallel\text{eq}}$ . The wave number of a par-  
 177 allel whistler mode wave in cold plasma can be approximated as (Stix, 1992)

$$178 \quad k = \frac{\omega}{c\chi\xi}, \quad \xi^2 \equiv \frac{1}{\chi^2} - 1 = \frac{\omega(\Omega_e - \omega)}{\omega_{\text{pe}}^2}. \quad (14)$$

179 As a consequence of Equations 7, 9, 11 and 14, the nonlinear growth rate  $\Gamma_N$  defined in  
 180 Equation 8 can be written explicitly as

$$181 \quad \Gamma_N = \frac{(2\xi\chi^3)^{\frac{1}{2}}QJ_{\text{E,max}}}{\gamma_R^{\frac{1}{2}}} \frac{\Omega_{\text{e0}}^2}{(\Omega_w\omega)^{\frac{1}{2}}} \left(\frac{\omega_{\text{phe}}}{\Omega_{\text{e0}}}\right)^2 \frac{V_g}{c} \left(\frac{V_{\perp 0}}{c}\right)^{\frac{5}{2}} \frac{c^2G}{N_{\text{he}}}, \quad (15)$$

182 showing a direct proportionality to  $\Omega_w^{-1/2}$ . The constant  $J_{\text{E,max}} \approx 0.98$  gives the value  
 183 of  $J_E = -J_{\text{E,max}}J_0$  at  $S = -S_{\text{max}}$  and can be obtained by numerically evaluating Equa-  
 184 tion 9.

185 The particles which interact with the whistler wave have velocities and gyrophases  
 186 that match the first order resonance condition for a wave whose spatio-temporal struc-  
 187 ture is given by  $\omega$  and  $k$ . Therefore, the particle bunches (and the depletion created by  
 188 the bunching) form a helical shape in space on which are imprinted the wave frequency  
 189 and wave vector of the interacting wave. Such helix can act as an antenna radiating a  
 190 right-hand circularly polarized wave on this frequency. The use of helical antennas for  
 191 creation of circularly polarized electromagnetic signals is a well-known concept in radio  
 192 science, proposed in the 1940s by Kraus (1949). To get an estimate on the strength of  
 193 the electromagnetic field radiated from the antenna, we will follow Yagitani et al. (1992)  
 194 who computed the electric field of L-mode and R-mode plasma waves radiated from a  
 195 current sheet on the background of a homogeneous magnetic field. Focusing on the R-  
 196 mode, we can rewrite the result of Yagitani et al. (1992) as

$$197 \quad E_{\delta}(z) = -\frac{c\mu_0}{2} \frac{\tilde{J}_s}{n} e^{-ik|z|}. \quad (16)$$

198 This is the response of the electric field to a current distribution given by  $\mathbf{J}_s = (\tilde{J}_s, 0, 0)\delta(z)$ ,  
 199 where  $\delta(z)$  is a delta distribution with units of inverse length and  $\tilde{J}_s$  has the units of cur-  
 200 rent density times length. Since we are not interested in the direction of the electric field  
 201 vector, we have simplified the formula by assuming that  $\mathbf{J}_s$  points along the  $x$ -axis, lead-  
 202 ing to  $E_{\delta}(z)$  having only one nonzero component in our coordinate system. To obtain

203 the field radiated by the helical resonant current, we just have to realize that the elec-  
 204 tric field,  $\mathbf{E}(z)$ , will always point in the direction of the current at each point along the  
 205  $z$ -axis, which coincides with the helical axis. Therefore, we only need to substitute the  
 206  $\delta$ -distribution with a more realistic distribution of the magnitude of the current. With  
 207 the resonant current distribution given as

$$208 \quad \mathbf{J}_R(z) = (\tilde{J}_R, 0, 0) \frac{1}{\sqrt{2\pi}\sigma_J} e^{-\frac{z^2}{2\sigma_J^2}}, \quad (17)$$

$$209 \quad \tilde{J}_R = \sqrt{2\pi}\sigma_J J_{\text{peak}}, \quad (18)$$

211 with  $\sigma_J$  being a characteristic width of the distribution, we can obtain the total radiated  
 212 field at a point  $z \rightarrow \infty$  (far enough from the antenna) by integrating over the current  
 213 distribution,

$$214 \quad E_{\text{tot}}(z) = -\frac{c\mu_0}{2} \frac{\tilde{J}_R}{n} e^{-ik|z|} \int_{-\infty}^{\infty} dz' \frac{1}{\sqrt{2\pi}\sigma_J} e^{-\frac{z'^2}{2\sigma_J^2}} = -\sqrt{\frac{\pi}{2}} c\mu_0 \frac{\sigma_J J_{\text{peak}}}{n} e^{-ik|z|}. \quad (19)$$

215 And since we have formulated the evolution equations in the terms of wave magnetic field,  
 216 we can now use the relation  $c|B_{\text{tot}}|/n = |E_{\text{tot}}|$  to obtain

$$217 \quad B_{\text{tot}} = -\sqrt{\frac{\pi}{2}} \mu_0 \sigma_J J_{\text{peak}}. \quad (20)$$

218 The quantity  $J_{\text{peak}}$  represents the peak value of the current density distribution, which  
 219 may be obtained from a numerical simulation.

220 With a uniform distribution of the current

$$221 \quad \mathbf{J}_R(z) = \begin{cases} (J_{\text{peak}}, 0, 0) & \text{for } -l/2 < z < l/2 \\ (0, 0, 0) & \text{otherwise} \end{cases} \quad (21)$$

222 we would get

$$223 \quad B_{\text{tot}} = -\frac{\mu_0}{2} l J_{\text{peak}}. \quad (22)$$

224 The strength of the magnetic field of the emitted wave is directly proportional to the length  
 225 of the helix. This is in agreement with the strength of electromagnetic field of circularly  
 226 polarized waves radiated from a helical antenna as derived by Kraus (1949), Eq. 27.

### 227 **2.3 Model of the subpacket structure**

228 We envision the formation of the subpacket structure of the whistler mode chorus  
 229 as follows. Initially, the electromagnetic emissions in the equatorial region are dominated  
 230 by incoherent noise. Through interaction with hot electrons, the amplitude of the noise

grows according to the linear growth theory with a rate  $\gamma_L$ , which maximizes at the equator, as it was shown by numerical simulations (Hikishima et al., 2009; Katoh & Omura, 2016). After a certain time the linear growth produces a coherent emission with a wave amplitude that reaches the threshold amplitude (Omura et al., 2009)

$$\Omega_{\text{thr}}(h_i) = \frac{5\xi\gamma_R s_2^2}{\chi^5 Q^2 J_{E,\text{max}} S_{\text{max}}} \frac{a^2 c^4}{\omega \Omega_{e0}^2} \left( \frac{\Omega_{e0}}{\omega_{\text{phe}}} \right)^4 \left( \frac{c}{V_{\perp 0}} \right)^7 \left( \frac{N_{\text{he}}}{c^2 G(h_i)} \right)^2, \quad (23)$$

where  $\omega_{\text{phe}}$  denotes the plasma frequency of hot electrons.  $\Omega_w > \Omega_{\text{thr}}$  expresses the necessary condition to start the nonlinear growth rate stage – below this threshold value, Equations 6 and 7 are not valid. Initially,  $\partial\omega/\partial t = 0$  and  $\partial\Omega_e/\partial h = 0$  at the equator, then  $S = 0$  as a consequence of Equation 3. Under such conditions, Equations 9 and 10 give  $J_E = 0$ , but  $J_B < 0$ . It has been shown by Omura and Nunn (2011) that the component  $J_B$  is related to the change of frequency  $\omega'$  across one whole subpacket by

$$\omega' = -\frac{\mu_0 V_g J_B}{2 B_w}. \quad (24)$$

The growth in frequency described by Equation 6 leads to the decrease of  $S$  and to the appearance of  $J_E$ , which maximizes for  $S = -S_{\text{max}}$ . Increase in  $J_E$  is followed by growth in amplitude as described by Equation 7. The emission also propagates away from the equator, experiencing further convective growth (Equation 2). The growth in the source is limited by the optimum amplitude (Omura & Nunn, 2011). As was the case with the first chorus equation (Equation 6), we need to include the shift of the source into the definition of the optimum amplitude. Let us introduce the ratio  $\tau = T_N/T_{\text{tr}}$  of the nonlinear transition time  $T_N$  for formation of the nonlinear resonant current, and the nonlinear trapping period

$$T_{\text{tr}} = \frac{2\pi}{\chi} \left( \frac{m_e \gamma_R}{k V_{\perp 0} e B_w} \right)^{\frac{1}{2}}. \quad (25)$$

Now we put forward an assumption that the optimum amplitude for nonlinear growth is reached when the frequency sweep rate over a trapping period  $\omega'/T_N$  is equal to the sweep rate  $\partial\omega/\partial t$  given by Equation 6. Since  $S = -S_{\text{max}}$  in the source, we have  $J_B = -J_{B,\text{max}} J_0$ , where  $J_{B,\text{max}} \approx 1.3$  can be obtained by numerical evaluation of Equation 10. With this assumption, we can use Equations 25, 24 and 6 to obtain the optimum amplitude

$$\Omega_{\text{opt}}(h_i) = \frac{J_{B,\text{max}} \chi^2 Q s_1}{2^{\frac{1}{2}} \pi S_{\text{max}} \gamma_R \tau s_0} \frac{\Omega_{e0}^2}{\omega} \left( \frac{\omega_{\text{phe}}}{\Omega_{e0}} \right)^2 \frac{V_g}{c} \left( \frac{V_{\perp 0}}{c} \right)^3 \frac{c^2 G(h_i)}{N_{\text{he}}} + \frac{2 a c h_i s_2}{S_{\text{max}} s_0} \frac{\Omega_{e0}}{\omega}. \quad (26)$$

After the wave amplitude reaches  $B_{\text{opt}}$ , the nonlinear growth mechanism breaks down. At the same time, the strongest resonant current is released into the upstream. As explained in Section 2.2, it forms a helical structure which continually radiates a whistler

263 mode wave at a frequency that matches the frequency of the initial wave at the point  
 264 where the current has been created, that is, a frequency  $\omega_1 = \omega_0 + \Delta\omega_1$ , where  $\omega_0$  is  
 265 the wave frequency of the initial subpacket and  $\Delta\omega_1$  is the frequency difference measured  
 266 at the point where the optimum amplitude was reached (point 1 in Figure 1). To model  
 267 a smooth decrease in amplitude of the initial subpacket, we simply switch the sign of the  
 268 right hand side of Equation 7. It is further assumed that the new wave, produced by the  
 269 radiation from the helical current, cannot replace the previous subpacket until its am-  
 270 plitude drops below  $B_{\text{thr}}$  (point 1'' in Figure 1). Using the group velocity  $V_g$  of the whistler  
 271 mode wave and the resonance velocity  $V_R$  of the particles, this corresponds to a wave  
 272 source located in the distance (point 1' in Figure 1)

$$\Delta h_1 = \frac{V_R V_g}{V_g - V_R} \Delta t_1, \quad (27)$$

274 starting at time

$$t_1 = (V_R t_{\text{max}} - V_g t_{\text{end}}) / (V_R - V_g). \quad (28)$$

276 The time interval between points 1'' and 1' was denoted  $\Delta t_1 = t_{\text{end}} - t_{\text{max}}$ . Since the  
 277 radiation emitted by the helical current is coherent, it is immediately subjected to the  
 278 nonlinear growth effects, provided it reaches the threshold amplitude. A new subpacket  
 279 is then established at  $\Delta h_1$  and the process repeats (points 2, 2', 2'' in Figure 1, etc.).  
 280 The flowchart of our model is sketched in Figure 2.

281 It will be shown later in Section 3.2 that the helical current can indeed be strong  
 282 enough to emit waves with amplitudes larger than the threshold value  $B_{\text{thr}}$ , based on  
 283 Equation 22 and simulated  $J_R$ . The simulation will also confirm that the ratio  $J_E/B_w$   
 284 from Equation 24 attains large values only near the source, suggesting that the nonlin-  
 285 ear frequency growth happens only in that region.

### 286 3 Numerical simulation

#### 287 3.1 Methods and initial conditions

288 We solve the partial differential equations 1 and 2 with an upwind integration scheme,  
 289 with the chorus Equations 6 and 7 acting as the boundary conditions at  $h_i$ . As the ini-  
 290 tial conditions we choose  $B_w(0, 0) \equiv B_{w0} = 2B_{\text{thr}}(0, 0)$  and  $\omega(0, 0) \equiv \omega_0 = 0.2\Omega_{e0}$ .  
 291 For each new subpacket the initial amplitude is always set to the double of the thresh-  
 292 old amplitude,  $B_w(h_i, t_i) = 2B_{\text{thr}}(h_i, t_i)$ , where  $h_i$  is obtained by adding up shifts de-  
 293 rived from Equation 27 and  $t_i$  is given by Equation 28. The process is stopped when  $B_{\text{thr}}(h_i) > B_{\text{opt}}(h_i)$

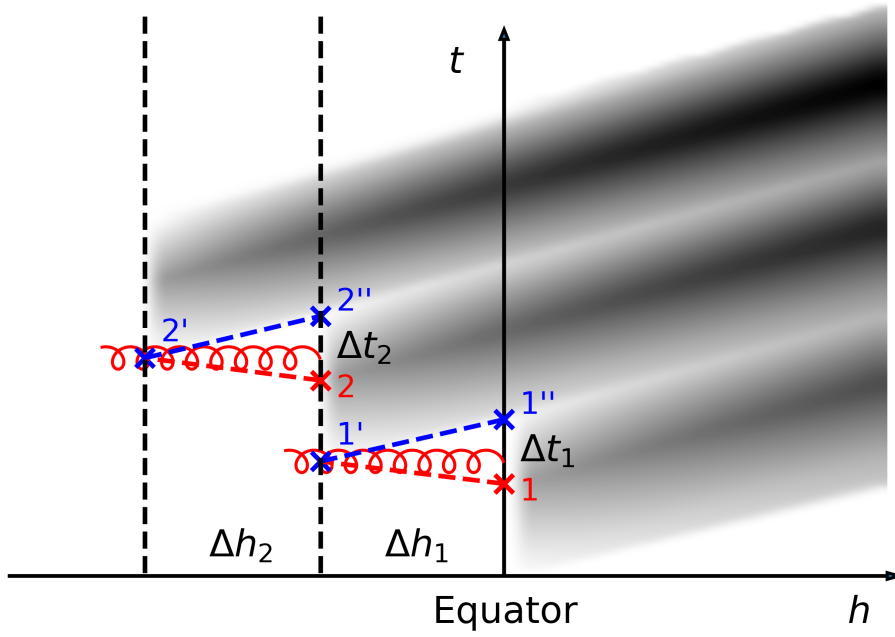


**Figure 1.** Schematic representation of the subpacket formation. After the wave amplitude reaches the optimum amplitude  $B_{\text{opt}}$  at point 1, it starts dropping until it reaches the threshold amplitude  $B_{\text{thr}}$  at point 1'' within a time period  $\Delta t_1$ . At this point the radiation emitted from point 1' arrives, where 1' corresponds with the peak helical current which was released from point 1. New subpacket starts growing from point 1'. This process is then repeated with each subpacket (points 2, 2' and 2'' etc.).

294 or when the initial frequency of the next subpacket exceeds a limiting frequency  $\omega_{\text{fin}} =$   
 295  $0.5 \Omega_{e0}$ . This cut-off at  $\omega_{\text{fin}}$  is necessary as there is no mechanism in our model that would  
 296 naturally confine the frequency to the lower band, like e.g. the nonlinear damping of oblique  
 297 waves at half the gyrofrequency (Omura et al., 2009).

### 298 3.2 Results

299 The Equations 1 and 2 are first solved for a set of parameters listed in Table 1 un-  
 300 der the row named "Mid". The chosen value of the magnetic field parameter  $a = 1.36 \cdot 10^{-7} c^{-2} \Omega_{e0}^2$   
 301 corresponds to an L-shell value of  $L = 4.5$  and equatorial gyrofrequency  $\Omega_{e0} = 6.0 \cdot 10^4 \text{ s}^{-1}$ ,  
 302 where we used the value  $3.1 \cdot 10^{-5} \text{ T}$  for the equatorial strength of the dipole field at the  
 303 surface of the Earth. The time step is set to  $t_{\text{step}} = 4 \Omega_{e0}^{-1}$  and the grid spacing is  $h_{\text{step}} = 1 c \Omega_{e0}^{-1}$ .

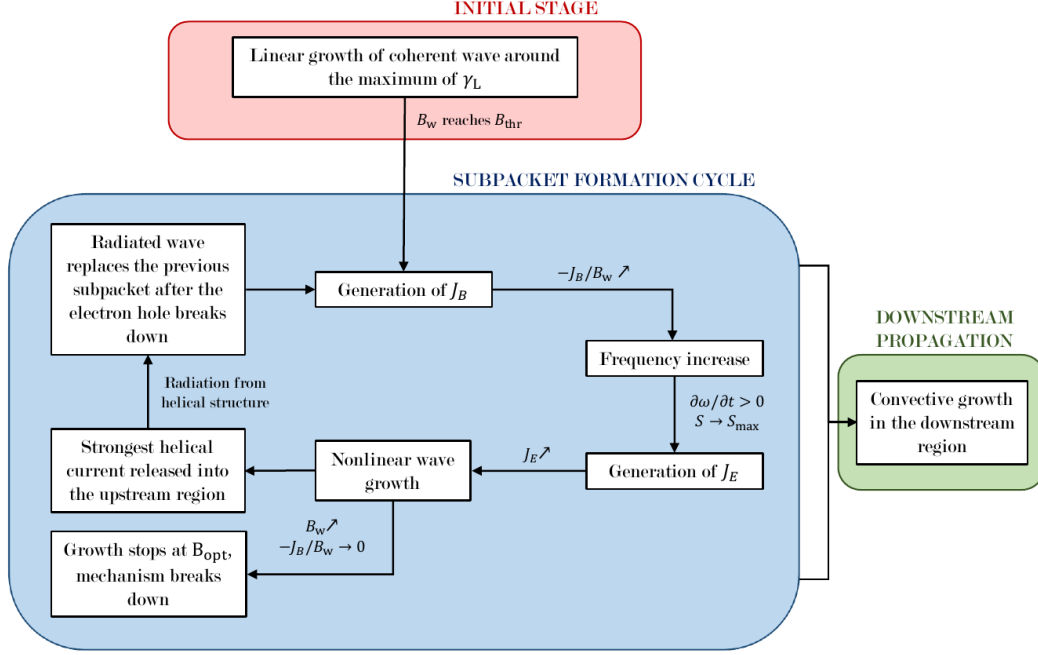


**Figure 2.** Flowchart of the formation process of the subpacket structure of a whistler mode chorus element.

304 In Figure 3 we present time-space plots of the wave frequency  $\omega$ , wave amplitude  $B_w$ ,  
 305 resonant current density  $J_R$  and its components  $J_E$ ,  $J_B$  and the ratio  $J_B/B_w$ . Accord-  
 306 ing to Equation 24, frequency growth should happen only where the  $J_B/B_w$  ratio plot-  
 307 ted in Figure 3f is large. This coincides with the source region, supporting thus the va-  
 308 lidity of our model. Figures 3c and 3d show that while the  $J_B$  component of the reso-  
 309 nant current density dominates in the downstream, it has values comparable to  $J_E$  close  
 310 to the source region. The peak values of the total resonant current density  $J_{peak}$  in the  
 311 source range from  $-0.39 \cdot 10^{-4} J_{norm}$  (first subpacket) to  $-1.06 \cdot 10^{-4} J_{norm}$  (last sub-  
 312 packet), where  $J_{norm} = m_e \Omega_{e0}^2 \mu_0^{-1} c^{-1} e^{-1}$  is a normalization factor. Following the scheme  
 313 in Figure 1, we take the peak value for the first subpacket and plug it into Equation 22  
 314 to calculate the strength of the magnetic field of the newly radiated wave. Assuming the  
 315 length of one loop of the helix  $l = 2\pi|V_R|/\Omega_{e0} = 1.65 c\Omega_{e0}^{-1}$ , we get  $B_{tot} = 3.2 \cdot 10^{-5} B_{eq}$ ,  
 316 which we can compare with the local threshold amplitude  $B_{thr} = 1.0 \cdot 10^{-6} B_{eq}$ . The  
 317 helical current can span over hundreds of loops, seemingly increasing the estimate by up  
 318 to two orders of magnitude. However, due to the frequency growth in the source, the pitch  
 319 of the helix is changing and so each section radiates at a different frequency, limiting thus

**Table 1.** Table with input and output parameters. Values in row "Mid" of the upper section of the table were used to produce the results in Figure 3, rows "Low" and "High" show alternate values for each of the parameters and rows "Set 1" and "Set 2" represent a set of values compiled from the three previous rows. Values in rows "Set 1" and "Set 2" were used to produce the results in Figure 4. The lower section of the table lists values of the following output parameters: number of subpackets  $N_S$ , upstream shift of the source  $h_{\text{elm}}$ , frequency sweep rate  $\Delta\omega/\Delta t$ , the time duration  $t_{\text{elm}}$ , the maximum amplitude  $B_{w,\text{max}}$  and the maximum frequency  $\omega_{\text{max}}$ . In this lower section, rows labeled as "Low" ("High") were obtained from simulations with input parameters from the "Mid" set of input parameters, but in each column we replaced the "Mid" value of the respective input parameter by its "Low" ("High") value. Values of the output parameters for the three sets of input values "Mid", "Set 1" and "Set 2" are shown in the three additional columns on the right side of the table. The sweep rate, the time duration and the maximum amplitude were always computed at a distance  $h = 500 c\Omega_{e0}^{-1}$ .

		$Q$	$\tau$	$\frac{\omega_{\text{pe}}}{\Omega_{e0}}$	$\frac{\omega_{\text{phe}}}{\Omega_{e0}}$	$\frac{V_{\perp 0}}{c}$	$\frac{U_{\text{th},\parallel\text{eq}}}{c}$	$\frac{a \cdot 10^7}{c^{-2}\Omega_{e0}^2}$			
	Mid	0.5	0.5	5.0	0.3	0.4	0.15	1.36			
	Low	0.25	0.25	4.0	0.2	0.3	0.12	0.86			
	High	1.0	1.0	6.0	0.4	0.5	0.20	3.07			
	Set 1	0.25	0.25	5.0	0.3	0.4	0.15	1.36			
	Set 2	0.5	1.0	6.0	0.4	0.4	0.20	0.86	Mid	Set 1	Set 2
$N_S$	Low	13	12	4	7	32	9	31	30	15	67
	High	24	142	30	25	28	29	26			
$h_{\text{elm}}$ km	Low	4400	1700	3300	3400	6700	3700	2800	3800	3700	2100
	High	1900	6500	2800	2200	2500	3200	6600			
$\left(\frac{\Delta\omega}{\Delta t}\right)$ kHz/s	Low	2.8	13.1	6.8	2.0	5.0	5.3	13.7	7.1	7.4	13.8
	High	12.4	4.8	7.8	11.2	9.8	8.2	2.5			
$t_{\text{elm}}$ ms	Low	310	220	30	220	580	100	300	400	400	300
	High	230	590	370	250	300	350	660			
$\frac{B_{w,\text{max}}}{B_{\text{eq}}}$ (%)	Low	0.6	2.2	0.3	0.4	0.8	0.5	1.5	1.5	1.1	1.4
	High	2.8	0.7	1.3	2.5	1.6	1.6	1.5			
$\frac{\omega_{\text{max}}}{\Omega_{e0}}$	Low	0.290	0.500	0.220	0.247	0.500	0.257	0.500	0.500	0.500	0.500
	High	0.500	0.500	0.500	0.500	0.500	0.500	0.500			

320 the spatial range we can use for our calculations. We will discuss this in more detail in  
 321 Section 5.

322 To show the effect of the model's parameters on the overall result, we increased or  
 323 decreased the values of the parameters one by one according to rows "Low" and "High"  
 324 in Table 1. We recorded the number of subpackets  $N_S$ , upstream shift of the source lo-  
 325 cation across the whole chorus element  $h_{\text{elm}}$ , the time duration  $t_{\text{elm}}$ , frequency sweep rate  
 326  $\Delta\omega/\Delta t$  and the maximum amplitude  $B_{w,\text{max}}$ . Sweep rate, time duration and maximum  
 327 amplitudes are calculated for  $h = 500 c\Omega_{e0}^{-1}$ , which is approximately equal to 2500 km  
 328 or to a magnetic latitude  $\lambda_m = 5^\circ$  for  $L = 4.5$ . If we measured the maximum ampli-  
 329 tudes at larger  $h$ , they would grow steadily up to unreasonable values ( $B_{w,\text{max}}/B_{\text{eq}} >$   
 330  $0.1$ ), which is caused by the assumption of parallel propagation of whistler modes, which  
 331 cannot be justified further from the equator, as was shown by systematic analysis of space-  
 332 craft measurements (Santolík, Macušová, et al., 2014) as well as by theoretical consid-  
 333 erations of chorus propagation in small ducts (Hanzelka & Santolík, 2019).

334 From a combination of values from the rows "Mid", "Low" and "High" in Table 1,  
 335 two new sets of parameters were assembled, "Set 1" and "Set 2", with the goal of ob-  
 336 taining a very low and a very high number of subpackets, while keeping the upstream  
 337 shift, time duration and maximum wave amplitude of the element at reasonably low val-  
 338 ues. The first set consists of "Low" values of  $\tau$  and  $Q$  and "Mid" values of the rest of  
 339 the parameters. The second set consists of a "Low" value of  $a$ , "Mid" values of  $Q$  and  
 340  $V_{\perp 0}$  and "High" values of  $\tau$ ,  $\omega_{pe}$ ,  $\omega_{phe}$  and  $U_{\text{th},\parallel\text{eq}}$ . The resulting time-space plots of wave  
 341 frequencies and amplitudes are presented in Figure 4. With the first set we managed to  
 342 push the number of subpackets down to  $N_S = 15$ , while with the second set a very large  
 343 value  $N_S = 66$  was obtained.

344 As we have seen in Section 2, most of the simulation parameters influence the model  
 345 in a highly complex manner. However, with the use of the results presented in Table 1  
 346 and Figure 3, we can observe some patterns. The effect of the parameter  $\tau$  is probably  
 347 the most obvious, as it is found only in the formula for the optimum amplitude, Equa-  
 348 tion 26. Low values of  $\tau$  give large optimum amplitudes, allowing the wave frequency  
 349 to grow more rapidly within one subpacket, which leads to a lower number of subpack-  
 350 ets and that in turn decreases the total upstream shift of the source. The time duration  
 351 is decreased due to the strong frequency growth as well. And naturally, higher maximum  
 352 amplitudes in the source result in higher amplitudes in the downstream. The influence  
 353 of the optimum amplitude on the results is visible also with the altered values of the other  
 354 model parameters, but it is combined with effects caused mainly by changes in  $J_E$  and  $B_{\text{thr}}$ .

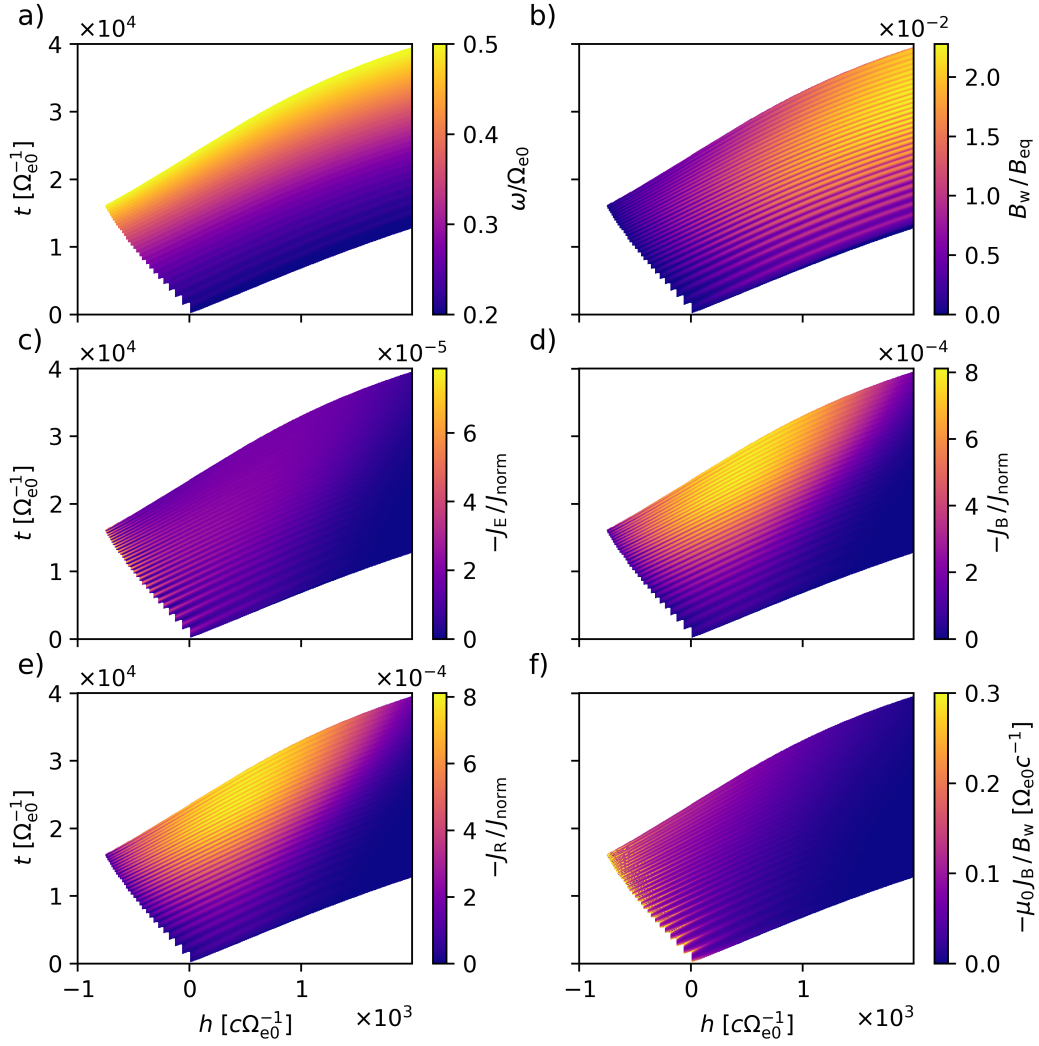


**Figure 3.** Evolution of the chorus element in time and space obtained with input parameter set "Mid" from Table 1. The equatorial gyrofrequency  $\Omega_{e0} = 6 \cdot 10^4 \text{ s}^{-1}$  can be used to convert the axis ranges to  $t = (0, 670) \text{ ms}$ ,  $h = (-5000, 10000) \text{ km}$  and to calculate  $J_{\text{norm}} = 5.4 \cdot 10^{-5} \text{ Am}^{-2}$ . The panels show in order a) wave frequency  $\omega$ , b) wave amplitude  $\Omega_w$ , c) resonant current density component  $-J_E$ , d) resonant current density component  $-J_B$ , e) total resonant current density  $-J_R$  and f) the ratio  $-J_B/B_w$ .

355 Increase/decrease in  $Q$  has the same qualitative effect as equivalent decrease/increase  
 356 in  $\tau$ , except for the low number of subpacket for small  $Q$  which is caused by the early  
 357 termination of the simulation due to low values of optimum amplitudes in the upstream.  
 358 Higher plasma frequency values can significantly decrease  $h_{\text{elm}}$ , but they have little ef-  
 359 fect on the other output parameters. Increased values of the density of hot plasma pop-

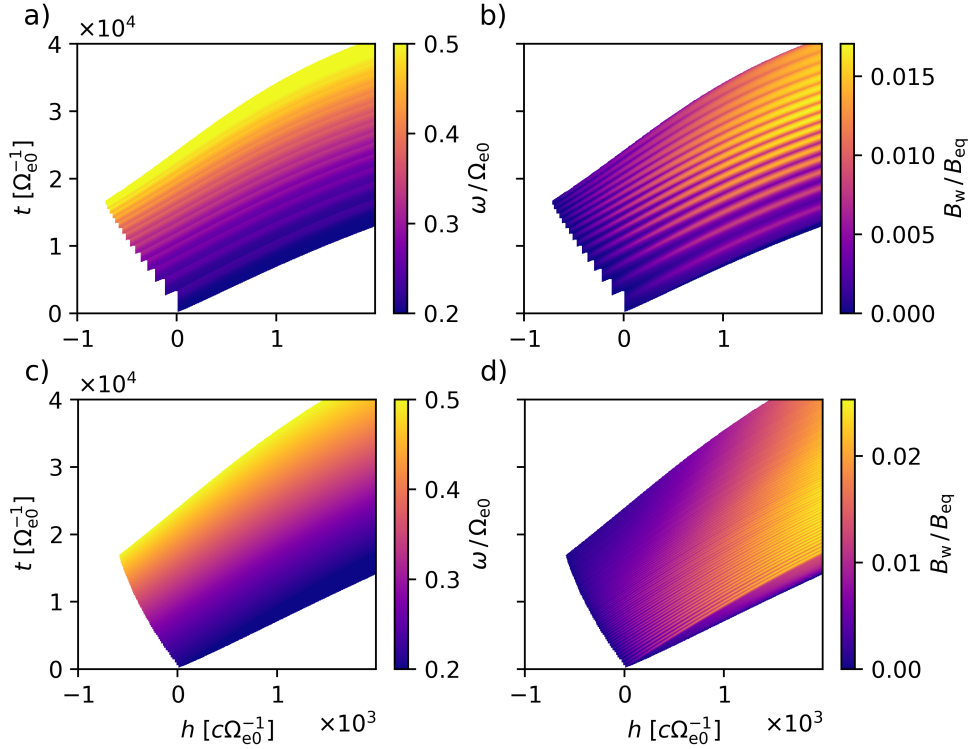


**Figure 4.** As in the first two panels of Figure 3, with panels a) and b) corresponding to parameters from "Set 1" and c) and d) to "Set 2". Due to the different L-shell value in the second pair of panels,  $L = 4.0$ , the axis ranges are  $t[\text{ms}] = (0, 530)$  and  $h[\text{km}] = (-3500, 7000)$  with  $\Omega_{e0} = 8.52 \cdot 10^4 \text{ s}^{-1}$ .

360 uation, expressed through  $\omega_{\text{phe}}$ , and perpendicular velocity  $V_{\perp 0}$ , affect the results qual-  
 361 itatively in the same way as an increase in  $Q$ . Low values of  $V_{\perp 0}$  can strongly increase  
 362 the drift of the source and the time duration of the element. The parallel thermal ve-  
 363 locity has the most complex influence due to its appearance in the exponential in Equa-  
 364 tion 12 as well as in the denominator of the formula, but the overall trend in the observed  
 365 resulting parameters is similar to the effect of  $\omega_{\text{phe}}$ . Finally, magnetic field inhomogene-  
 366 ity parameter  $a$  can strongly influence the sweep rate and the drift of the source.

367 To better understand what the chorus element could look like in the measurements  
 368 of a stationary spacecraft, we plot the time evolution of wave frequency and amplitude  
 369 in Figure 5 for the three sets of parameters "Mid", "Set 1" and "Set 2". The position  
 370 in space is fixed to latitudes of  $5^\circ$  (red lines) and  $15^\circ$  (blue lines). In Figures 5a and 5c  
 371 we can clearly see frequency drops between adjacent subpackets, while in panel e) this

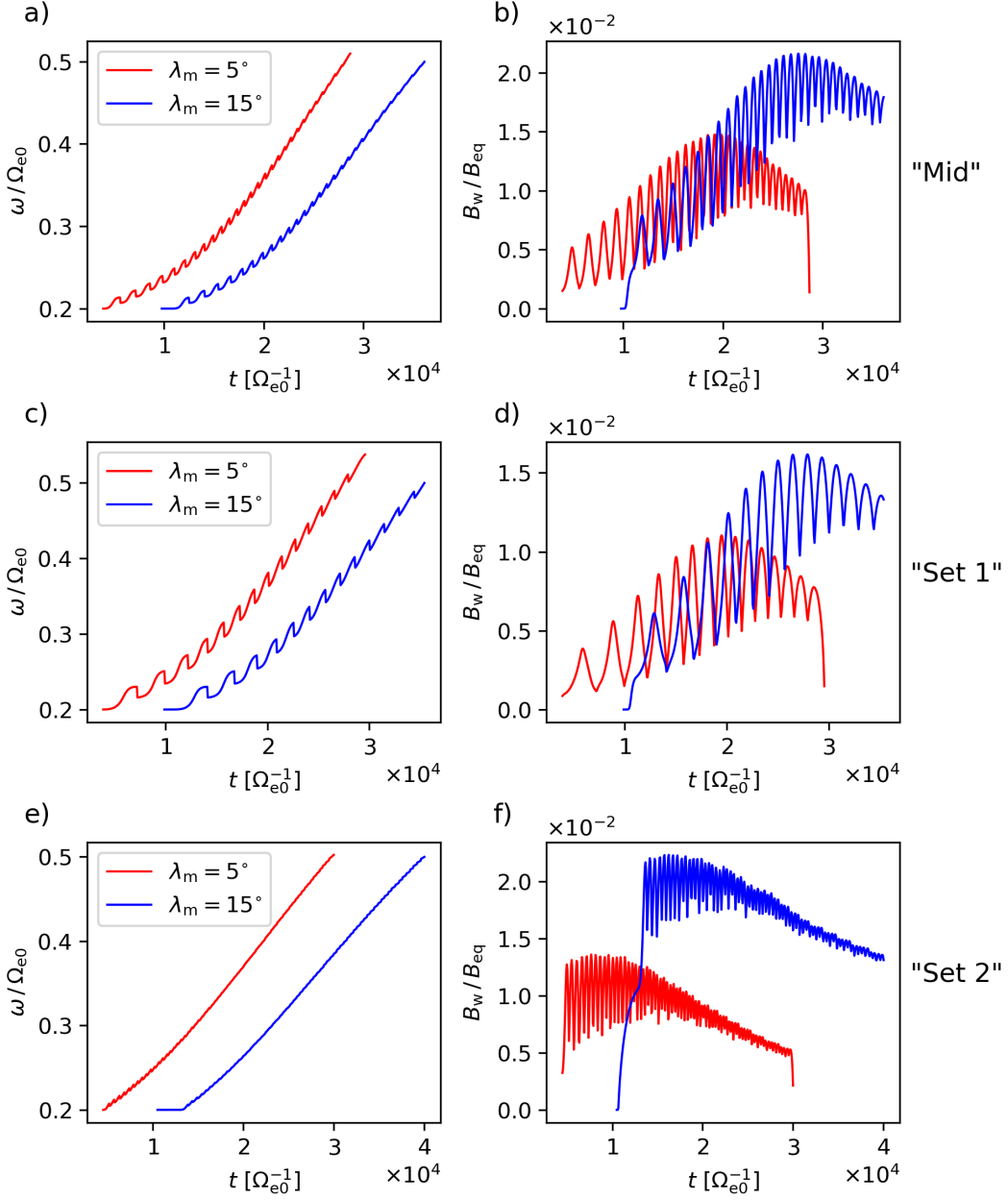


**Figure 5.** Wave frequencies and amplitudes for the three different sets of parameters "Mid" (a,b), "Set 1" (c,d) and "Set 2" (e,f). The data are specified at latitudinal distance  $5^\circ$  (red lines) and  $15^\circ$  (blue lines).

372 behavior becomes indistinct due to the large number of subpackets in the fine structure.  
 373 Also, with rising frequency the subpackets are getting shorter and the ratios between the  
 374 increase and the following drop in frequency within one subpacket are decreasing. The  
 375 envelope of the amplitudes follows the dependence of the optimum amplitude on frequency

376 (see e.g. Omura and Nunn (2011), Figure 3a for comparison). With rising frequencies  
 377 the peaks in the amplitude plot are getting smoother due to increasing dispersion of the  
 378 whistler mode waves propagating in cold plasma. Dispersion also causes decrease of the  
 379 relative height of the peak (from base to top), making the fine structure more homoge-  
 380 neous.

381 Last but not least, we have tested the influence of the initial value of the wave am-  
 382 plitude of each subpacket. We determined that as long as the threshold amplitude  $B_{\text{thr}}$   
 383 is by at least one order of magnitude smaller than the optimum amplitude  $B_{\text{opt}}$ , any ini-  
 384 tial amplitude that ranges from about  $1.5 B_{\text{thr}}$  to  $3.0 B_{\text{thr}}$  has negligible effect on the re-  
 385 sults of the simulation. Similarly, decreasing integration steps in space and time by half  
 386 did not lead to any changes in the values of output parameters.

#### 387 4 Comparison with observation

388 High quality electromagnetic wave measurements provided by the two Van Allen  
 389 Probes were used to identify large amplitude chorus events in the radiation belts. One  
 390 such event, detected by the Van Allen Probe B spacecraft on 12 September 2014, is pre-  
 391 sented in Figure 6. Figures 6a and 6b respectively show the frequency-time power spec-  
 392 trograms obtained from the magnetic field and the electric field measurements, recorded  
 393 by the EMFISIS Waves instrument (Kletzing et al., 2013) in the morning sector at McIl-  
 394 wain's  $L = 5.61$  and magnetic latitude  $\lambda_m = 5.24^\circ$  northward from the magnetic equa-  
 395 tor. A sequence of intense chorus elements is clearly seen in both spectrograms below  
 396 one half of the local electron cyclotron frequency, which is shown as a white or black solid  
 397 line on the spectrograms. These electromagnetic waves have a right-hand circular po-  
 398 larization, indicating the presence of the whistler mode in Fig. 6c obtained using the method  
 399 of Santolík et al. (2002).

400 The planarity of the magnetic polarization obtained by the singular value decom-  
 401 position (SVD) method (Santolík, Parrot, & Lefeuvre, 2003), plotted in Fig. 6d, is above  
 402 0.8 in the lower frequency parts of the elements between 1.2 kHz and 1.5 kHz, correspond-  
 403 ing to the presence of a single plane wave in a given frequency-time bin of the spectro-  
 404 gram. The planarity is below 0.8 in the upper frequency parts of the elements extend-  
 405 ing up to a frequency of 1.7 kHz, suggesting that the plane wave approximation should  
 406 not be used above 1.5 kHz.

407 The angle  $\theta_k$  between the wave vector and local magnetic field line is lower than  
 408  $10^\circ - 20^\circ$  below 1.5 kHz, as shown in Fig. 6e. The higher values observed at larger fre-  
 409 quencies are not reliable under the plane wave assumption. The azimuth of the wave vec-  
 410 tor in Fig. 6f shows a predominant outward propagation in the plane of the local mag-  
 411 netic meridian. Finally, Fig. 6g shows that spectral estimates of the Poynting vector, ob-  
 412 tained using a method of Santolík et al. (2010), give directions outward from the mag-  
 413 netic equator.

414 The data recorded in the burst mode of the EMFISIS Waves instrument have a sam-  
 415 pling rate of 35 kHz and a 16-bit dynamic range, allowing thus for a detailed analysis of  
 416 the fine structure of chorus. Figures 7a and 7b show detailed waveforms of the first cho-  
 417 rus element from Fig. 6. The analysis method used in Figures 7c, 7d and 7e is similar  
 418 to the method used for measurements of the Cluster mission by Santolík et al. (2004)  
 419 and the same as the analysis procedure used for another interval of Van Allen Probes  
 420 measurements by Santolík, Kletzing, et al. (2014): The calibrated waveform is pass-band  
 421 filtered between 0.4 kHz and 3 kHz and analytic signals are constructed using the Hilbert  
 422 transform. Their instantaneous amplitudes are shown in Fig. 7c. The instantaneous fre-  
 423 quencies plotted in Fig. 7d are obtained as time derivatives of the phases of the complex  
 424 analytic signals, while both the instantaneous phases and amplitudes are used to con-  
 425 struct instantaneous spectral matrices, whose SVD analysis provides us with estimates  
 426 of the instantaneous wave vector angles plotted in Fig 7e.

427 The analyzed chorus element is composed of subpackets, in consistence with the  
 428 assumptions made in the model described in Section 2.3. The instantaneous frequency  
 429 is globally rising with time but sometimes it steps back at the boundaries of the subpack-  
 430 ets. This is consistent with the simulation results in Section 3. The input and output  
 431 parameters analyzed in Table 1 cannot be readily compared with the observation since  
 432 we do not measure  $Q$  and  $\tau$ , which have both strong influence on the output parame-  
 433 ters. Also, the assumption of bi-Maxwellian distribution, included in equations 12 and 13,  
 434 need not hold, making the parameters  $V_{\perp 0}$  and  $U_{th,||eq}$  hard to interpret. Nevertheless,  
 435 we can still look at the properties of the analyzed element and see that the parameters  
 436  $N_S \approx 23$ ,  $\Delta\omega/\Delta t \approx 1.8$  kHz/s and  $t_{elm} \approx 400$  ms are within a multiple of 2 from the  
 437 output parameters obtained in the simulation with  $a = 3.07 \cdot 10^{-7} c^{-2} \Omega_{e0}$ , which cor-  
 438 responds to  $L = 5.5$ .

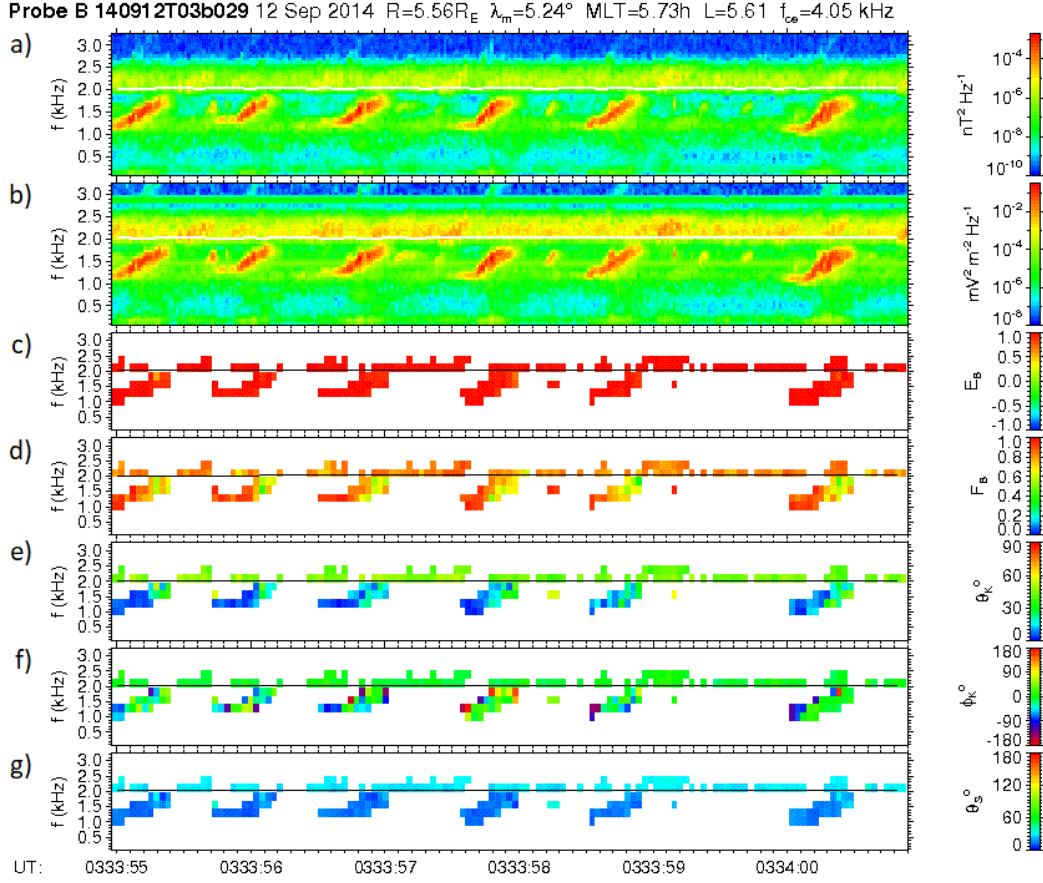


**Figure 6.** Results of spectral analysis of multicomponent measurements recorded by the EMFISIS Waves instrument on Van Allen Probe B on 12 September 2014. Frequency-time spectrograms of a) sum of the power spectral densities of the magnetic components, b) sum of the power spectral densities of the electric components c) ellipticity of the magnetic field polarization with a sign corresponding to the sense of polarization, d) planarity of the magnetic field polarization, e) angle between the wave vector and the background magnetic field, f) azimuth of the wave vector with respect to the outward direction in the plane of the local magnetic meridian, and g) angle between the Poynting vector and the background magnetic field. A color scale is given on the right-hand side of each spectrogram. One half of the local electron cyclotron frequency is given by a white or black solid line in each plot. Time is given in UT at the bottom.

439 Figure 7 clearly shows that the waveforms of the perpendicular and parallel com-  
 440 ponents behave differently, their subpacket structure is different and their estimated in-  
 441 stantaneous frequencies are also slightly different. This is strongly reflected by the in-  
 442 stantaneous wave vector angle which changes its value within each subpacket. As it was

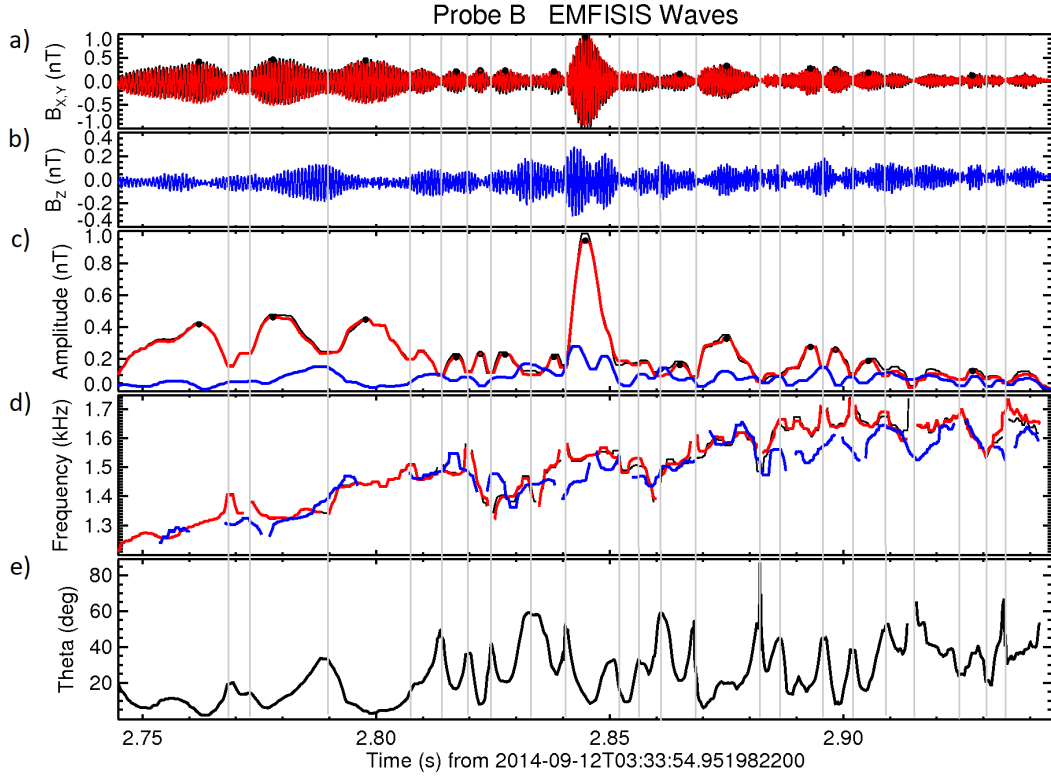


**Figure 7.** Detailed analysis of the first chorus element from Figure 6. a) Waveform of magnetic field fluctuations perpendicular to the local field line, b) waveform of the magnetic field fluctuations along the field line, c) instantaneous amplitudes for the perpendicular and parallel components and for the modulus, shown respectively by red, blue, and black lines, d) instantaneous frequency with the same color coding plotted for the instantaneous amplitudes larger than 50 pT, e) instantaneous angle between the wave vector and the local field line; vertical grey lines show the minima of amplitude of the dominant perpendicular component; black dots show its local maxima larger than 50 pT relative to adjacent minima.

443

already noted for another case analyzed by Santolík, Kletzing, et al. (2014), the amplitude maxima generally correspond to the minima of the instantaneous wave vector angle.

444

445

## 5 Discussion and conclusion

446

447

In the development of our model of the fine structure of rising tone chorus emission, we decided to base it on the nonlinear growth theory described in Omura et al. (2008) and the follow-up papers. There exists another prominent theory of the chorus emission,

448

449

450 summarized e.g. in Trakhtengerts (1999), which is based on the backward oscillator regime  
 451 of cyclotron masers in space. It has been successfully applied to explain the time delay  
 452 between chorus elements and their frequency sweep rate (Demekhov (2017) and refer-  
 453 ences therein), but it has not yet explained their fine structure.

454 A crucial role in the subpacket formation process is played by the electromagnetic  
 455 radiation emitted from the resonant electrons leaving the source region. We have shown  
 456 that the emitted wave should be theoretically far above the threshold amplitude, pos-  
 457 sibly even reaching the optimum amplitude, which would stop the nonlinear growth mech-  
 458 anism. However, the computation relied on the current having a shape of a perfect he-  
 459 lix. In reality, the magnitude of the current is dependent on the phase bunching process.  
 460 Without phase bunching of the untrapped resonant electrons, there is no net current.  
 461 Therefore we should introduce a new parameter,  $0 < P < 1$ , which would represent  
 462 the quality of phase bunching and control the strength of the magnetic field of the emit-  
 463 ted whistler wave as a multiplicative factor on the right hand side of Equation 20 or 22.  
 464 Such parameter could be obtained through test-particle simulations of electrons trav-  
 465 eling through the potential of a whistler mode wave. In full-particle simulations, the ra-  
 466 diation appears naturally in the solution of Maxwell equations for the particle system.

467 Another effect that can decrease the power of the emitted wave is the changing pitch  
 468 of the helix. As the frequency of the wave inside the primary subpacket continuously in-  
 469 creases, the helical current must copy the structure and change its pitch. This would lead  
 470 to broadening of the spectral peak of the emitted wave, and to decrease of its maximum  
 471 power. Since the amplitude of the current in the source has a peak (see Figure 3e, also  
 472 compare with amplitude peaks in Fig. 5b which partially copy the evolution of current),  
 473 we do not expect this effect to be very prominent. Nevertheless, it is clear that the true  
 474 nature of this radiation process is more complex than shown in our model. Another ap-  
 475 proach to the antenna effect can be found in Trakhtengerts et al. (2003), where they com-  
 476 pute the radiated power and frequency shift directly from the transport equations for  
 477 the wave amplitude and nonlinear phase. Since they do not consider any subpacket struc-  
 478 ture, the antenna length becomes much longer and dephasing starts to play a major role.  
 479 They conclude that the frequency shift due to the antenna effect should be about 100 Hz  
 480 in typical magnetospheric conditions, which is similar to our result, and that the ampli-  
 481 tude of the new wave  $B_w/B_{eq}$  is between  $10^{-5}$  and  $10^{-4}$ , which is above the threshold  
 482 amplitudes considered in this paper.

483 The comparison of simulation results with observations of the Van Allen Probes  
 484 confirms that the drops in frequency between subpackets, which are a fundamental part  
 485 of our model, can be observed in large amplitude chorus elements. The upstream shift  
 486 of the source, which is another important feature of the model, cannot be determined  
 487 from measurements of a single spacecraft, but indirect indications of a similar effect have  
 488 been reported by Taubenschuss et al. (2017) for bidirectional chorus wave packets. Two  
 489 satellites with a small spatial separation (hundreds of kilometers) should be in princi-  
 490 ple able to directly intercept one chorus element inside the source at different stages of  
 491 its development. If this proposed drift of the source were real, one satellite (at the equa-  
 492 tor) would see the whole frequency range of the element, while the other one (shifted slightly  
 493 upstream) would see only the upper part of the range, and the first coherent, large am-  
 494 plitude emission would appear with a significant time delay with respect to the first satel-  
 495 lite’s measurement. Short distances between spacecraft with highly sensitive wave in-  
 496 struments were achieved during several close separation campaigns of the four-spacecraft  
 497 Cluster mission (see e.g. Němec et al. (2014)), and additional work is needed to iden-  
 498 tify signatures of this effect for special configurations when different spacecraft are lo-  
 499 cated close to a single magnetic field line, at transverse separations lower than a typi-  
 500 cal transverse size of generation regions of separate chorus wave packets, i.e. on the or-  
 501 der of 100 km according to Santolík and Gurnett (2003) and Santolík et al. (2004).

502 The only simulation that clearly showed and analyzed a shift of the source region  
 503 within a nonlinear theory was the simulation of EMIC waves by Shoji and Omura (2013),  
 504 where the upstream drift of the source was qualitatively similar to our chorus simula-  
 505 tion, but we cannot make any quantitative comparison due to the different nature of the  
 506 whistler waves and ion cyclotron waves. Some less well-behaved movement of the source  
 507 has been observed in chorus simulations as well, e.g. in the full-particle simulations of  
 508 Hikishima and Omura (2012), but it was not properly discussed there.

509 Another point that must be mentioned in the discussion of our results is the choice  
 510 of ranges of parameter values which we used in simulations. While the field inhomogene-  
 511 ity  $a$  is given by the dipole field model and plasma frequency  $\omega_{pe}$  can be chosen based  
 512 on measurements in the equatorial region of the outer radiation belt, the choice of the  
 513 remaining parameters is less obvious. The most important constraint imposed on the pa-  
 514 rameters is that  $B_{thr} \ll B_{opt}$  must hold for the initial frequency. Our goal was to keep  
 515 the values of  $\omega_{phe}$ ,  $V_{\perp 0}$  and  $U_{th,\parallel eq}$  as low as possible, because in general, very hot and

516 dense distributions are less likely to occur. Since all our simulations started at frequency  
 517  $\omega = 0.2 \Omega_{e0}$ , i.e. at a fairly low value, we had to settle for hot plasma frequency of about  
 518  $0.3 \Omega_{e0}$ , which corresponds to relative density  $n_{\text{hot}}/n_{\text{cold}} = 3.6 \cdot 10^{-3}$  for  $\omega_{pe} = 5.0 \Omega_{e0}$ .  
 519 This is because the ratio  $B_{\text{thr}}/B_{\text{opt}}$  increases rapidly as the wave frequency decreases,  
 520 as was shown by Omura and Nunn (2011). Even with these high hot electron densities,  
 521 a small change of parameters could lead to large drifts of the source, which can cause  
 522 the optimum amplitude to decrease below the threshold amplitude. This is demonstrated  
 523 in Table 1, where the maximum frequency  $\omega_{\text{max}}$  does not always reach the limiting fre-  
 524 quency  $\omega_{\text{fin}}$ , resulting in very short chorus elements. The quantities  $Q$  and  $\tau$  are essen-  
 525 tially free parameters of the nonlinear growth theory, since they cannot be estimated with-  
 526 out performing a self-consistent simulation, and therefore can be used to tweak the re-  
 527 sults to certain extent.

528 One of the consequences of the rather high values of hot plasma density are the large  
 529 overall amplitudes of resulting whistler waves, reaching typically a few percent of the back-  
 530 ground magnetic field (Figure 5). These results are overestimated because we have lim-  
 531 ited our study to parallel propagation. The  $\theta_k$  values can also reach tens of degrees in-  
 532 side the source region (Santolík et al., 2009). Even in cases where the propagation is glob-  
 533 ally quasiparallel (Figure 6) the  $\theta_k$  values vary at time scales of subpackets (Santolík,  
 534 Kletzing, et al., 2014), as we can also see in Figure 7. Energy of oblique whistler waves  
 535 is transferred back to electrons through the Landau resonance (Hsieh & Omura, 2018),  
 536 decreasing thus the observed wave amplitudes. The two dimensional nature of the cho-  
 537 rus emission also has significant influence on the particle acceleration, as was shown by  
 538 Omura et al. (2019). Crabtree et al. (2017) even suggest that the chorus generation mech-  
 539 anism is inherently three dimensional, as they discovered a smooth change in the azimuthal  
 540 angle of the wave vector within single subpackets.

541 To summarize, we have shown that a model based on the nonlinear growth theory  
 542 and the antenna effect can be used to simulate growth and propagation of single cho-  
 543 rus elements with subpacket structure. The model features steep drops in frequency at  
 544 the point where one subpacket transitions to the next one, and an upstream drift of the  
 545 source region with increasing wave frequency. The first feature was confirmed by obser-  
 546 vations of the Van Allen Probes spacecraft, the second one appears in self-consistent par-  
 547 ticle simulations. Time duration and frequency sweep rate of the element and the num-  
 548 ber of subpackets obtained through simulations are comparable to those observed in a

549 typical event of intense chorus recorded by the Van Allen Probe B spacecraft. The model  
 550 can be used in test particle simulations to determine the effect of subpackets on parti-  
 551 cle acceleration – this is left for future studies.

## 552 Acknowledgments

553 M. Hanzelka, I. Kolmašová and O. Santolík acknowledge support from the Premium Academiae  
 554 award, the Mobility Plus grant JSPS 1905, and the INTER-EXCELLENCE program,  
 555 grant No. LTAUSA17070. M. Hanzelka acknowledges support from the Charles Univer-  
 556 sity through the Mobility Fund, project No. FM/c/2019-1-004, and thanks the Research  
 557 Institute for Sustainable Humanosphere of the Kyoto University for hosting his visit to  
 558 Uji in summer 2019. Work at the Kyoto University was supported by JSPS KAKENHI  
 559 grant No. 15H05815 and No. 17H06140. The authors sincerely thank the Van Allen Probes/EMFISIS  
 560 team for their work on the design and tests of the flight hardware and for conducting  
 561 the operations and archiving work which provided us with the continuous waveform data  
 562 used in this study and stored on <https://emfisis.physics.uiowa.edu/>. The data used to  
 563 produce plots in Figures 3, 4 and 5 were obtained by solving numerically Equations 1  
 564 and 2 and are available for download at [http://babeta.ufa.cas.cz/repository/jgr\\_](http://babeta.ufa.cas.cz/repository/jgr_chorus_2020_wave_data.zip)  
 565 [\\_chorus\\_2020\\_wave\\_data.zip](http://babeta.ufa.cas.cz/repository/jgr_chorus_2020_wave_data.zip).

## 566 References

- 567 Crabtree, C., Tejero, E., Ganguli, G., Hospodarsky, G. B., & Kletzing, C. A. (2017).  
 568 Bayesian spectral analysis of chorus subelements from the van allen probes.  
 569 *Journal of Geophysical Research (Space Physics)*, *122*(6), 6088-6106. doi:  
 570 10.1002/2016JA023547
- 571 Demekhov, A. G. (2017, Mar). Relationship Between the Parameters of the Lin-  
 572 ear and Nonlinear Wave Generation Stages in a Magnetospheric Cyclotron  
 573 Maser in the Backward-Wave Oscillator Regime. *Radiophysics and Quantum*  
 574 *Electronics*, *59*(10), 773-781. doi: 10.1007/s11141-017-9746-6
- 575 Dysthe, K. B. (1971, Oct). Some studies of triggered whistler emissions. *Journal of*  
 576 *Geophysical Research*, *76*(28), 6915-6931. doi: 10.1029/JA076i028p06915
- 577 Foster, J. C., Erickson, P. J., Omura, Y., Baker, D. N., Kletzing, C. A., & Claude-  
 578 pierre, S. G. (2017, Jan). Van Allen Probes observations of prompt MeV  
 579 radiation belt electron acceleration in nonlinear interactions with VLF cho-

- 580 rus. *Journal of Geophysical Research (Space Physics)*, 122(1), 324-339. doi:  
581 10.1002/2016JA023429
- 582 Hanzelka, M., & Santolik, O. (2019, Jun). Effects of Ducting on Whistler Mode  
583 Chorus or Exohiss in the Outer Radiation Belt. *Geophysical Research Letters*,  
584 46(11), 5735-5745. doi: 10.1029/2019GL083115
- 585 Helliwell, R. A. (1967, Oct). A theory of discrete VLF emissions from the magne-  
586 tosphere. *Journal of Geophysical Research*, 72(19), 4773-4790. doi: 10.1029/  
587 JZ072i019p04773
- 588 Hikishima, M., & Omura, Y. (2012, Apr). Particle simulations of whistler-  
589 mode rising-tone emissions triggered by waves with different amplitudes.  
590 *Journal of Geophysical Research (Space Physics)*, 117(A4), A04226. doi:  
591 10.1029/2011JA017428
- 592 Hikishima, M., Omura, Y., & Summers, D. (2010, Dec). Self-consistent particle sim-  
593 ulation of whistler mode triggered emissions. *Journal of Geophysical Research*  
594 (*Space Physics*), 115(A12), A12246. doi: 10.1029/2010JA015860
- 595 Hikishima, M., Yagitani, S., Omura, Y., & Nagano, I. (2009, January). Full par-  
596 ticle simulation of whistler-mode rising chorus emissions in the magne-  
597 tosphere. *Journal of Geophysical Research (Space Physics)*, 114, A01203. doi:  
598 10.1029/2008JA013625
- 599 Hsieh, Y.-K., & Omura, Y. (2018, Sep). Nonlinear Damping of Oblique Whistler  
600 Mode Waves Via Landau Resonance. *Journal of Geophysical Research (Space*  
601 *Physics)*, 123(9), 7462-7472. doi: 10.1029/2018JA025848
- 602 Kasahara, Y., Miyoshi, Y., Omura, Y., Verkhoglyadova, O. P., Nagano, I., Kimura,  
603 I., & Tsurutani, B. T. (2009, Jan). Simultaneous satellite observations of VLF  
604 chorus, hot and relativistic electrons in a magnetic storm “recovery” phase.  
605 *Geophysical Research Letters*, 36(1), L01106. doi: 10.1029/2008GL036454
- 606 Katoh, Y., & Omura, Y. (2016, November). Electron hybrid code simulation  
607 of whistler-mode chorus generation with real parameters in the Earth’s in-  
608 ner magnetosphere. *Earth, Planets and Space*, 68, 192. doi: 10.1186/  
609 s40623-016-0568-0
- 610 Kletzing, C. A., Kurth, W. S., Acuna, M., MacDowall, R. J., Torbert, R. B.,  
611 Averkamp, T., ... Tyler, J. (2013, Nov). The Electric and Magnetic Field  
612 Instrument Suite and Integrated Science (EMFISIS) on RBSP. *Space Science*

- 613            *Reviews*, 179(1-4), 127-181. doi: 10.1007/s11214-013-9993-6
- 614 Kraus, J. D. (1949). The Helical Antenna. *Proceedings of the IRE*, 37, 263-272.
- 615 Kurita, S., Katoh, Y., Omura, Y., Angelopoulos, V., Cully, C. M., Le Contel, O., &  
616 Misawa, H. (2012, November). THEMIS observation of chorus elements with-  
617 out a gap at half the gyrofrequency. *Journal of Geophysical Research (Space*  
618 *Physics)*, 117, A11223. doi: 10.1029/2012JA018076
- 619 Lighthill, M. J. (1965, Jan). Group Velocity. *Journal of the Institute of Mathematics*  
620 *and Its Applications*, 1, 1-28.
- 621 Nakamura, S., Omura, Y., Shoji, M., Nosé, M., Summers, D., & Angelopoulos, V.  
622 (2015, Sep). Subpacket structures in EMIC rising tone emissions observed by  
623 the THEMIS probes. *Journal of Geophysical Research (Space Physics)*, 120(9),  
624 7318-7330. doi: 10.1002/2014JA020764
- 625 Nunn, D. (1974, Mar). A self-consistent theory of triggered VLF emissions. *Plane-*  
626 *tary and Space Science*, 22(3), 349-378. doi: 10.1016/0032-0633(74)90070-1
- 627 Němec, F., Pickett, J. S., & Santolík, O. (2014, November). Multispacecraft Clus-  
628 ter observations of quasiperiodic emissions close to the geomagnetic equa-  
629 tor. *Journal of Geophysical Research (Space Physics)*, 119, 9101-9112. doi:  
630 10.1002/2014JA020321
- 631 Omura, Y., Hikishima, M., Katoh, Y., Summers, D., & Yagitani, S. (2009, Jul).  
632 Nonlinear mechanisms of lower-band and upper-band VLF chorus emissions in  
633 the magnetosphere. *Journal of Geophysical Research (Space Physics)*, 114(A7),  
634 A07217. doi: 10.1029/2009JA014206
- 635 Omura, Y., Hsieh, Y.-K., Foster, J. C., Erickson, P. J., Kletzing, C. A., & Baker,  
636 D. N. (2019, Apr). Cyclotron Acceleration of Relativistic Electrons Through  
637 Landau Resonance With Obliquely Propagating Whistler-Mode Chorus Emis-  
638 sions. *Journal of Geophysical Research (Space Physics)*, 124(4), 2795-2810.  
639 doi: 10.1029/2018JA026374
- 640 Omura, Y., Katoh, Y., & Summers, D. (2008, April). Theory and simulation of the  
641 generation of whistler-mode chorus. *Journal of Geophysical Research (Space*  
642 *Physics)*, 113, A04223. doi: 10.1029/2007JA012622
- 643 Omura, Y., & Nunn, D. (2011, May). Triggering process of whistler mode cho-  
644 rus emissions in the magnetosphere. *Journal of Geophysical Research (Space*  
645 *Physics)*, 116(A5), A05205. doi: 10.1029/2010JA016280

- 646 Omura, Y., Pickett, J., Grison, B., Santolík, O., Dandouras, I., Engebretson, M.,  
 647 ... Masson, A. (2010, Jul). Theory and observation of electromagnetic ion  
 648 cyclotron triggered emissions in the magnetosphere. *Journal of Geophysical*  
 649 *Research (Space Physics)*, *115*(A7), A07234. doi: 10.1029/2010JA015300
- 650 Omura, Y., & Summers, D. (2006, Sep). Dynamics of high-energy electrons  
 651 interacting with whistler mode chorus emissions in the magnetosphere.  
 652 *Journal of Geophysical Research (Space Physics)*, *111*(A9), A09222. doi:  
 653 10.1029/2006JA011600
- 654 Santolík, O., Gurnett, D., & Pickett, J. (2004, July). Multipoint investigation of the  
 655 source region of storm-time chorus. *Annales Geophysicae*, *22*, 2555-2563. doi:  
 656 10.5194/angeo-22-2555-2004
- 657 Santolík, O., & Gurnett, D. A. (2003, Jan). Transverse dimensions of chorus in  
 658 the source region. *Geophysical Research Letters*, *30*(2), 1031. doi: 10.1029/  
 659 2002GL016178
- 660 Santolík, O., Gurnett, D. A., Pickett, J. S., Chum, J., & Cornilleau-Wehrlin, N.  
 661 (2009, Dec). Oblique propagation of whistler mode waves in the chorus source  
 662 region. *Journal of Geophysical Research (Space Physics)*, *114*(A12), A00F03.  
 663 doi: 10.1029/2009JA014586
- 664 Santolík, O., Gurnett, D. A., Pickett, J. S., Parrot, M., & Cornilleau-Wehrlin, N.  
 665 (2003, July). Spatio-temporal structure of storm-time chorus. *Journal of*  
 666 *Geophysical Research (Space Physics)*, *108*, 1278. doi: 10.1029/2002JA009791
- 667 Santolík, O., Gurnett, D. A., Pickett, J. S., Parrot, M., & Cornilleau-Wehrlin,  
 668 N. (2004, Jan). A microscopic and nanoscopic view of storm-time cho-  
 669 rus on 31 March 2001. *Geophysical Research Letters*, *31*(2), L02801. doi:  
 670 10.1029/2003GL018757
- 671 Santolík, O., Kletzing, C. A., Kurth, W. S., Hospodarsky, G. B., & Bounds, S. R.  
 672 (2014, January). Fine structure of large-amplitude chorus wave packets. *Geo-*  
 673 *physical Research Letters*, *41*, 293-299. doi: 10.1002/2013GL058889
- 674 Santolík, O., Macúšová, E., Kolmašová, I., Cornilleau-Wehrlin, N., & Conchy, Y.  
 675 (2014, April). Propagation of lower-band whistler-mode waves in the outer  
 676 Van Allen belt: Systematic analysis of 11 years of multi-component data from  
 677 the Cluster spacecraft. *Geophysical Research Letters*, *41*, 2729-2737. doi:  
 678 10.1002/2014GL059815

- 679 Santolík, O., Parrot, M., & Lefeuvre, F. (2003, February). Singular value decompo-  
 680 sition methods for wave propagation analysis. *Radio Science*, *38*, 10-1. doi: 10  
 681 .1029/2000RS002523
- 682 Santolík, O., Pickett, J. S., Gurnett, D. A., Menietti, J. D., Tsurutani, B. T., &  
 683 Verkhoglyadova, O. (2010, July). Survey of Poynting flux of whistler mode  
 684 chorus in the outer zone. *Journal of Geophysical Research (Space Physics)*,  
 685 *115*, A00F13. doi: 10.1029/2009JA014925
- 686 Santolík, O., Pickett, J. S., Gurnett, D. A., & Storey, L. R. O. (2002, Dec). Mag-  
 687 netic component of narrowband ion cyclotron waves in the auroral zone.  
 688 *Journal of Geophysical Research (Space Physics)*, *107*(A12), 1444. doi:  
 689 10.1029/2001JA000146
- 690 Shoji, M., & Omura, Y. (2013, Sep). Triggering process of electromagnetic ion cy-  
 691 clotron rising tone emissions in the inner magnetosphere. *Journal of Geophysi-  
 692 cal Research (Space Physics)*, *118*(9), 5553-5561. doi: 10.1002/jgra.50523
- 693 Stix, T. (1992). *Waves in Plasmas*. Melville NY: American Institute of Physics.
- 694 Summers, D., Omura, Y., Miyashita, Y., & Lee, D.-H. (2012, Sep). Nonlinear spa-  
 695 tiotemporal evolution of whistler mode chorus waves in Earth's inner magne-  
 696 tosphere. *Journal of Geophysical Research (Space Physics)*, *117*(A9), A09206.  
 697 doi: 10.1029/2012JA017842
- 698 Summers, D., Tang, R., Omura, Y., & Lee, D.-H. (2013, Jul). Parameter spaces for  
 699 linear and nonlinear whistler-mode waves. *Plasma Physics*, *20*(7), 072110. doi:  
 700 10.1063/1.4816022
- 701 Tao, X., Bortnik, J., Albert, J. M., Thorne, R. M., & Li, W. (2013, July). The im-  
 702 portance of amplitude modulation in nonlinear interactions between electrons  
 703 and large amplitude whistler waves. *Journal of Atmospheric and Terrestrial  
 704 Physics*, *99*, 67-72. doi: 10.1016/j.jastp.2012.05.012
- 705 Taubenschuss, U., Demekhov, A. G., & Santolik, O. (2017, Jan). Interpretation of  
 706 whistler mode chorus observations with the backward wave oscillator model. In  
 707 *Planetary radio emissions viii* (p. 233-242). doi: 10.1553/PRE8s233
- 708 Trakhtengerts, V. Y. (1999, January). A generation mechanism for chorus emission.  
 709 *Annales Geophysicae*, *17*, 95-100. doi: 10.1007/s00585-999-0095-4
- 710 Trakhtengerts, V. Y., Demekhov, A. G., Hobara, Y., & Hayakawa, M. (2003).  
 711 Phase-bunching effects in triggered vlf emissions: Antenna effect. *Journal of*

- 712            *Geophysical Research (Space Physics)*, 108(A4). doi: 10.1029/2002JA009415
- 713 Tsurutani, B. T., & Smith, E. J.    (1974, Jan).    Postmidnight chorus: A substorm  
714            phenomenon.    *Journal of Geophysical Research*, 79(1), 118-127.    doi: 10.1029/  
715            JA079i001p00118
- 716 Tsurutani, B. T., Verkhoglyadova, O. P., Lakhina, G. S., & Yagitani, S. (2009, Mar).  
717            Properties of dayside outer zone chorus during HILDCAA events: Loss of en-  
718            energetic electrons.    *Journal of Geophysical Research (Space Physics)*, 114(A3),  
719            A03207. doi: 10.1029/2008JA013353
- 720 Turner, D. L., Angelopoulos, V., Li, W., Hartinger, M. D., Usanova, M., Mann,  
721            I. R., ... Shprits, Y.    (2013, May).    On the storm-time evolution of rela-  
722            tivistic electron phase space density in Earth's outer radiation belt.    *Jour-  
723            nal of Geophysical Research (Space Physics)*, 118(5), 2196-2212.    doi:  
724            10.1002/jgra.50151
- 725 Yagitani, S., Habagishi, T., & Omura, Y.    (2014, Jun).    Geotail observation of up-  
726            per band and lower band chorus elements in the outer magnetosphere.    *Jour-  
727            nal of Geophysical Research (Space Physics)*, 119(6), 4694-4705.    doi: 10.1002/  
728            2013JA019678
- 729 Yagitani, S., Nagano, I., Omura, Y., & Matsumoto, H.    (1992, Aug).    Comparison  
730            between particle simulation and full-wave analysis for wave propagation in a  
731            nonuniform plasma.    *Radio Science*, 27(4), 449-462. doi: 10.1029/92RS00854